



# Micro-modulation of linkers of covalent organic frameworks as catalysts for $2e^-$ oxygen reduction reaction

Xuwen Li<sup>a,b,c,1</sup>, Yubin Fu<sup>d,1</sup>, Qizheng An<sup>e,1</sup>, Shuai Yang<sup>f</sup>, Xiubei Yang<sup>b,c</sup>, Qing Xu<sup>b,c,\*</sup>, Gaofeng Zeng<sup>b,c,\*</sup>, Zheng Jiang<sup>e,\*\*</sup>

<sup>a</sup> Shanghai Institute of Applied Physics, Chinese Academy of Science, Shanghai 201210, PR China

<sup>b</sup> University of Chinese Academy of Sciences, Beijing 100049, PR China

<sup>c</sup> CAS Key Laboratory of Low-Carbon Conversion Science and Engineering, Shanghai Advanced Research Institute (SARI), Chinese Academy of Sciences (CAS), Shanghai 201210, PR China

<sup>d</sup> Center for Advancing Electronics Dresden (cfaed) & Faculty of Chemistry and Food Chemistry, Technische Universität Dresden, Dresden 01062, Germany

<sup>e</sup> National Synchrotron Radiation Laboratory, University of Science and Technology of China, Hefei 230029, PR China

<sup>f</sup> School of Physical Science and Technology, Shanghai Tech University, Shanghai 201210, PR China

## ARTICLE INFO

### Keywords:

Covalent organic frameworks  
Linker engineering  
Metal-free catalysts  
Oxygen reduction reaction  
Atomic modulation

## ABSTRACT

Covalent organic frameworks (COFs) are attractive as metal-free catalysts for the  $2e^-$  oxygen reduction reaction (ORR) owing to their tunable skeletons and porosities. However, the specific roles of their properties, such as crystallinity, porosity, dipole moment, and binding ability to reactants, in the catalytic performance are still unknown. In this work, we adopted a linker engineering strategy to reveal the crucial factors in determining the catalytic performance. The properties of the COFs were systematically engineered by altering the substituent groups in the linkers. The optimized Br-COF achieved a maximum selectivity of 86.2%, and a mass activity of  $32.0 \text{ A g}^{-1}$ , which were 112% and 174% higher than those from unmodified COF, respectively. The experimental and theoretical results revealed that the reductive ability of the COFs exerted the most prominent effect on their catalytic activity and confirmed that the easy formation of an  $\text{OOH}^*$  intermediate contributed to the high activity.

## 1. Introduction

Covalent organic frameworks (COFs) are a class of designable porous polymers that are constructed with various building blocks linked by covalent bonds.[1–5] By varying the building blocks, COFs with various dimensional topologic skeletons and controllable pore shapes and sizes can be obtained.[6–10] In addition to the tailored geometric structures, COFs also exhibit high functional tunability.[11–15] Thus, depending on the functional groups that are integrated in the frameworks or along the porous interfaces, COFs have found application in gas absorption, water harvesting, light-emission, photodetection, photocatalysis, ionic conduction, and energy storage and conversion.[16–20] Notably, by integrating different electrocatalytic sites in the skeletons or the porous interfaces, COFs have been utilized as electrocatalysts for the oxygen reduction reaction (ORR), water splitting, and carbon dioxide reduction

[21–26].

Electrochemical synthesis of hydrogen peroxide plays an important role in energy systems and many efforts have been made to develop heteroatom-doped carbon-based catalysts with high selectivity and activity.[27,28] However, it is difficult to precisely control their doping degree, defect level and active site location at the molecular level. COFs offer an ideal template for the construction of highly efficient catalysts for the electrocatalytic  $2e^-$  ORR owing to their predictable distributed site location, coordination environment, and controllable porosities.[29–36] Since 2020, Chen et al., unambiguously revealed the trend of different metal centers in intrinsically electrocatalytic M-N-C SACs with broad pH activity towards  $\text{H}_2\text{O}_2$ . [37] Zeng et al., demonstrated the use of metal-immobilized sites along pore channels for electrocatalytic  $\text{H}_2\text{O}_2$  synthesis. [38] In addition to metal-contained COFs, metal-free COFs with different heteroatoms have also been shown to catalyze the  $2e^-$

\* Corresponding authors at: University of Chinese Academy of Sciences, Beijing 100049, PR China.

\*\* Corresponding author.

E-mail addresses: [xuqing@sari.ac.cn](mailto:xuqing@sari.ac.cn) (Q. Xu), [zenggf@sari.ac.cn](mailto:zenggf@sari.ac.cn) (G. Zeng), [jiangz@ustc.edu.cn](mailto:jiangz@ustc.edu.cn) (Z. Jiang).

<sup>1</sup> These authors contribute equally to this work

ORR.[39–43] Wang et al., synthesized a highly stable imidazole-conjugated fully conjugated three-dimensional covalent organic framework as a metal-free catalyst via a saddle-shaped, one-pot, multicomponent Debus-Radziszewski reaction, exhibiting excellent semiconducting properties and metal-free, non-carbonated two-electron oxygen reduction reaction (ORR) electrocatalytic activity.[44] Segura et al., proposed a new method allowing room temperature and scalable synthesis of highly fluorinated to synthesize COFs for electrosynthesis of hydrogen peroxide.[45] However, COFs exhibit different topologies, surface areas, crystallinity, dipole moments, O<sub>2</sub> binding ability, and reductive ability, hindering the identification of the precise effects of such properties on the catalytic performance.[46,47] For example, COFs with different trigonal nodes possessing distinct electron configurations catalyze the ORR with different results in terms of activity and selectivity. Moreover, one-dimensional COFs bearing C=N linkages display higher catalytic activity than 2D derivatives.[48] Thus, elucidating the specific features of COFs that enable the 2e<sup>−</sup> ORR catalytic activity is essential for the design of highly active catalysts with tunable catalytic properties.

Herein, we adopted a linker engineering strategy to modulate the electronic states of COFs and investigate their effect on the 2e<sup>−</sup>-ORR catalytic performance. Upon varying the electronic nature of the substituents in the linkers, COFs having similar crystal skeletons, porosities, and stability but tunable electronic features were obtained (Fig. 1A), thus enabling the modulation of the catalytic performance. In particular, introducing Br atoms in the linkers resulted in improved activity via formation of an OOH\* intermediate.

## 2. Experimental section

Synthesis of PYTA-TP-COF (H-COF): PYTA-TP-COF was synthesized

by PYTA (0.03 mmol, 17 mg), TP (0.06 mmol, 8.05 mg), n-butanol (0.5 mL) and o-dichlorobenzene (0.5 mL) in a Pyrex tube measuring 10 × 8 mm (o.d × i.d), which was then sonication for 10 min to obtain a uniform solution. Then, the aqueous acetic acid (0.1 mL, 6 M) was added to the mixed solution. The tube was frozen at 77 K in a liquid N<sub>2</sub> bath and degassed by three freeze–pump–thaw cycles. The tubes were then vacuum sealed and heated at 120 °C for 72 h. The powders was filtered, further washed with tetrahydrofuran and dried at 80 °C under 50 mTorr for 12 h yield the product (85%).

Synthesis of other R-COFs: The linkers with different groups were used in the synthesis process to yield R-COFs by same methods. (Details of other synthesized COFs in [supporting information](#)).

## 3. Results and discussion

### 3.1. Characterizations of COFs

First, the basal COF (H-COF) without substituents was synthesized using 4,4',4'',4'''-(1,5a1-dihydropyrene-1,3,6,8-tetrayl)tetraaniline (PYTA) as the knots and terephthalaldehyde (TP) as the linker via a previously reported solvothermal method.[49] Then, a series of COFs (R-COFs) bearing electron-donating (R = OH, OCH<sub>3</sub>, and CH<sub>3</sub>) and electron-withdrawing (R = Br, Cl, and F) groups in the linkers were prepared using the same synthesis conditions (Fig. 1 A).

The Fourier transform infrared (FTIR) spectra of the synthesized COFs showed a band attributable to the C=N linkages at 1621 cm<sup>−1</sup>, confirming the successful synthesis of the linkages (Fig. S1). Moreover, bands corresponding to C-F, C-Cl, C-Br, C-OH, C-CH<sub>3</sub>, and C-OCH<sub>3</sub> were observed at 1142, 744, 621, 1209, 1519, and 1219 cm<sup>−1</sup>, respectively. Thus, COFs with designable building units were successfully constructed.

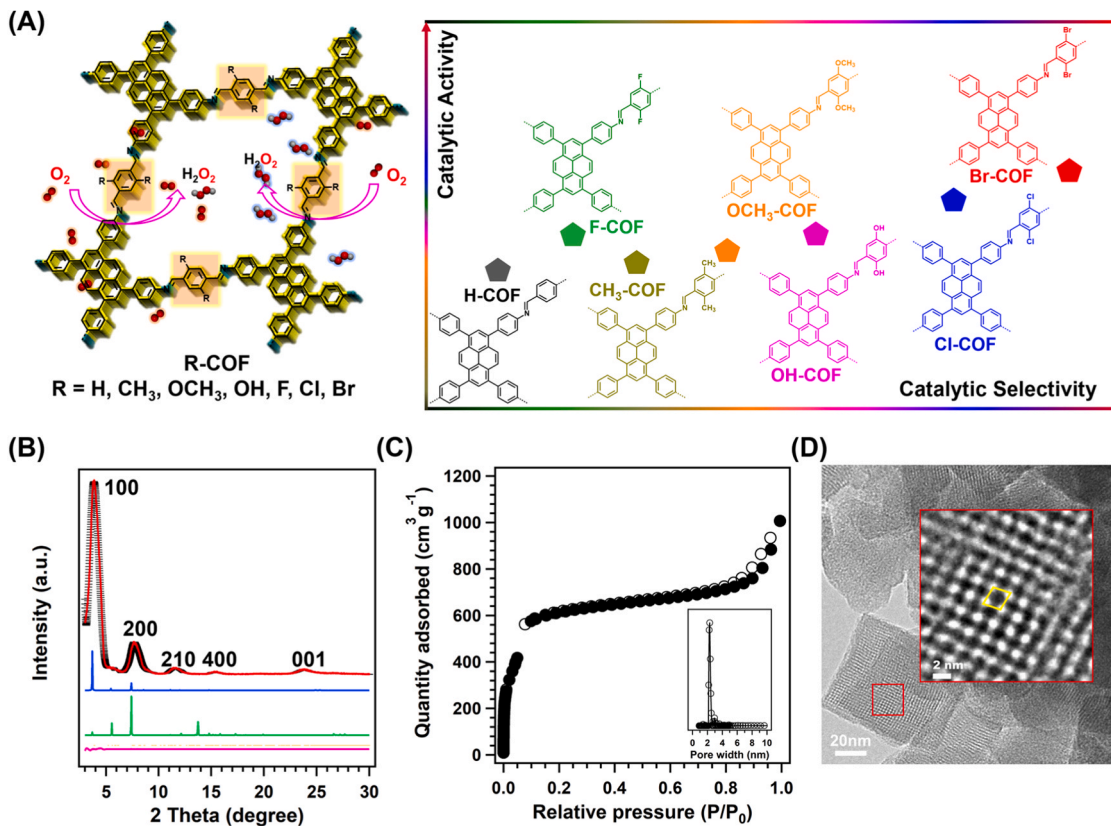


**Fig. 1.** (A) Constructing COFs for 2e<sup>−</sup> ORR via linker engineering. (B) Experimental (black) and Pawley refined (red) powder X-ray diffraction (PXRD) profiles of H-COF, and their different (pink) Bragg positions (orange) simulated using the AA (blue) and staggered AB (green) stacking modes. (C) N<sub>2</sub> sorption isotherms at 77 K and pore size distribution curves (insert) of H-COF. (D) High-resolution transmission electron microscopy (TEM) image of H-COF.

The crystal frameworks of all the synthesized COFs were explored by performing powder X-ray diffraction (PXRD) measurements. The PXRD pattern of H-COF showed 100, 200, 210, 400, and 001 facets at  $3.84^\circ$ ,  $7.65^\circ$ ,  $11.4^\circ$ ,  $15.4^\circ$ , and  $23.7^\circ$ , respectively (Fig. 1B). Pawley refinements showed there is little difference between the experimental and theoretical values,  $R_{wp}$  is 7.94% and  $R_p$  is 5.49%, respectively. The AA and AB stacking models of the COFs were simulated, and the AA stacking model was in good agreement with the experimental results (Fig. S2 and Tables S1). Slight differences were observed in the most intense peaks corresponding to the 100 facets of the COFs with different linkers, i.e., Br-COF, Cl-COF, OH-COF, OCH<sub>3</sub>-COF, F-COF, and CH<sub>3</sub>-COF, which appeared at  $3.84^\circ$ ,  $3.88^\circ$ ,  $3.88^\circ$ ,  $3.92^\circ$ ,  $4.08^\circ$ , and  $3.88^\circ$ , respectively (Fig. 2A). The peaks from the 001 facets were observed at  $23.94^\circ$ ,  $23.96^\circ$ ,  $23.98^\circ$ ,  $24.35^\circ$ ,  $23.82^\circ$  and  $24.07^\circ$ , respectively, indicating that the interlayer spaces in the COFs did not change upon the introduction of substituents. The full width at half maximum (FWHM) of the (100) peaks of H-COF was 1.07 (Fig. S3), smaller than Br-COF (1.44), Cl-COF

(1.54), F-COF (1.36), OH-COF (1.27), CH<sub>3</sub>-COF (1.24), and slightly larger than OCH<sub>3</sub>-COF (1.04), suggesting that introducing different groups in the linkers resulted in slight lower crystallinity [50].

The porous structure of H-COF was investigated by measuring the N<sub>2</sub> sorption isotherms at 77 K, finding that H-COF exhibited a BET surface area of  $2085 \text{ m}^2 \text{ g}^{-1}$  (Fig. 1C). Meanwhile, the pore size distribution curves showed that the pore volume and pore size of H-COF were  $1.25 \text{ cm}^3 \text{ g}^{-1}$  and  $2.30 \text{ nm}$ , respectively. The substituted COFs showed type-I(b) sorption isotherms, which were indicative of their small mesopore domain. [51,52] In particular, the BET surface areas decreased to 1770, 1490, 1460, 1317, 1222, and  $1123 \text{ m}^2 \text{ g}^{-1}$  for OH-COF, F-COF, OCH<sub>3</sub>-COF, Cl-COF, Br-COF, and CH<sub>3</sub>-COF, respectively, relative to that of H-COF (Fig. 2B and S4). The pore size distribution curves revealed that all the COFs contained pores with the same size of  $\sim 2 \text{ nm}$  (Fig. 2C and S5) and volumes of 1.01, 0.93, 1.13, 0.92, 0.99, and  $0.92 \text{ cm}^3 \text{ g}^{-1}$  for OH-COF, F-COF, OCH<sub>3</sub>-COF, Cl-COF, Br-COF, and CH<sub>3</sub>-COF, respectively (Fig. S6).

The morphologies of the COFs were studied via scanning electron

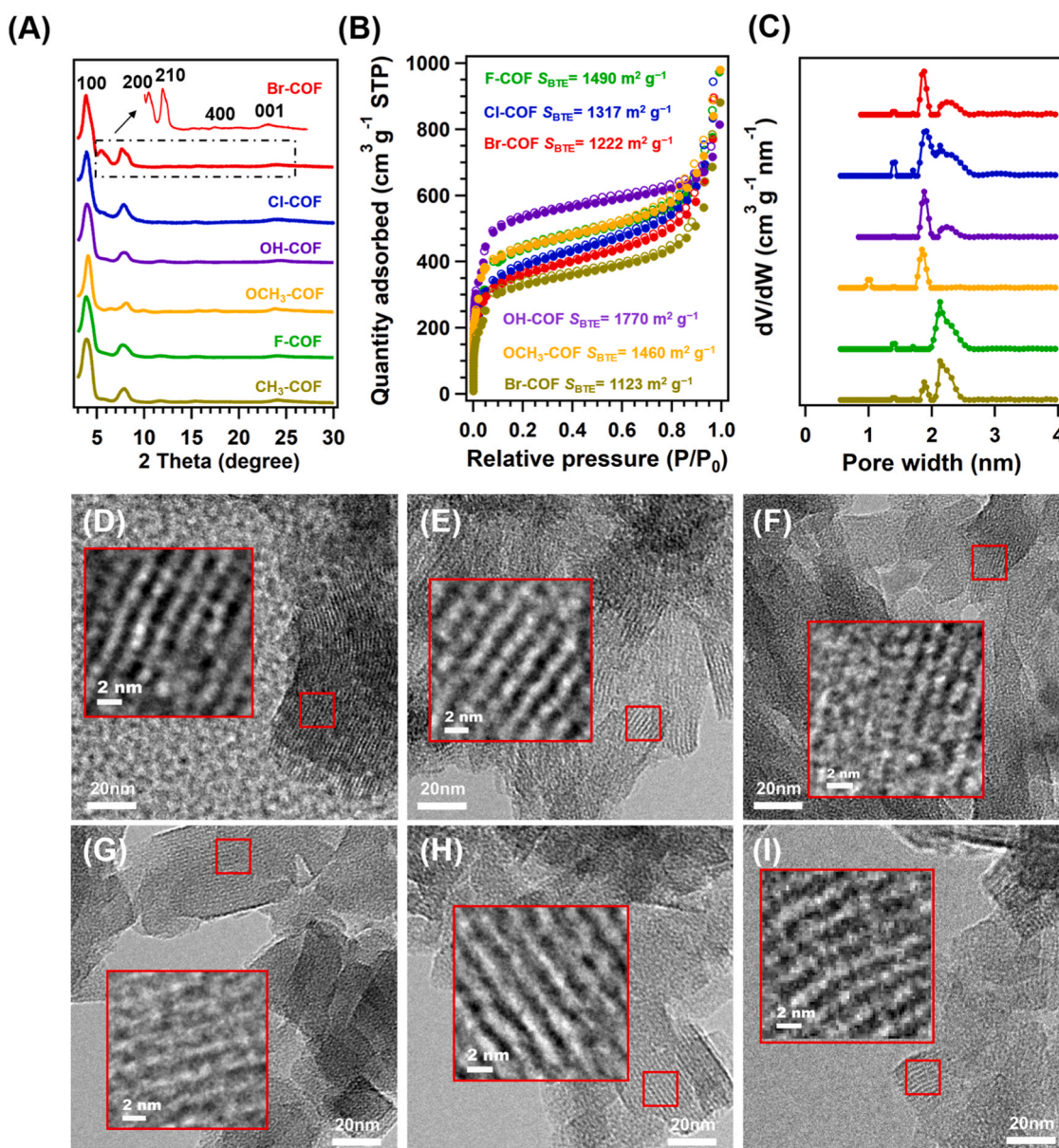


**Fig. 2.** (A) The PXRD Profiles, inset: magnified patterns of  $2\theta = 4.8\text{--}30^\circ$  and (B) N<sub>2</sub> sorption isotherms at 77 K, and (C) pore size distribution curves for Br-COF, Cl-COF, F-COF, OH-COF, OCH<sub>3</sub>-COF, and CH<sub>3</sub>-COF. High-resolution transmission electron microscopy (TEM) images of (D) Br-COF, (E) Cl-COF, (F) F-COF, (G) OH-COF, (H) OCH<sub>3</sub>-COF, and (I) CH<sub>3</sub>-COF.

microscopy (SEM) and transmission electron microscopy (TEM). The SEM (Fig. S7) and TEM images (Fig. S8–14) of all the COFs showed similar cube-shaped crystals. The energy-dispersive X-ray mapping images showed a uniform distribution of all the elements in the skeletons (Fig. S15). In the high-resolution TEM images of the COFs, ordered and open pores in different directions were observed, which further confirmed their highly ordered skeletons and porous channels (Figs. 1D and 2D–I).

X-ray photoelectron spectroscopy (XPS) was used to reveal the different electron states of the COFs. All the elements in the COFs were detected in the XPS spectra, and the C weight contents in Br-COF, Cl-COF, F-COF, OH-COF, OCH<sub>3</sub>-COF, CH<sub>3</sub>-COF, and H-COF were determined to be 84.60%, 84.05%, 84.81%, 84.50%, 84.91%, 88.79%, and 89.18%, respectively (Fig. S16). The C 1s XPS spectrum of H-COF in Fig. 3A displayed three peaks at 284.7, 285.3 and 286.2 eV, which can

be assigned to the binding energies of C=C, C=N, and C-N, respectively. [53] And the relative contents of 62.9%, 27.7%, and 9.4%, respectively. The high-resolution XPS C 1s spectra confirmed the different electronic states of the C atoms in the COFs. The C-Br, C-Cl, C-F, C-O, C-OCH<sub>3</sub>, and C-C bonds afforded peaks at 286.7, 286.8, 287.4, 287.2, 287.2, and 284.7 eV, respectively, with relative contents of 4.1%, 5.1%, 8.9%, 3.2%, and 9.1%, respectively. [54,55] The high-resolution of N 1s were further analyzed. Meanwhile, the high-resolution XPS N 1s spectra of all COFs showed two peaks at 399.2 and 400.3 eV that can be assigned to C=N and C-N, with the same contents of ~80% and ~20% (Fig. 3B).

Solid-state nuclear magnetic resonance (NMR) <sup>13</sup>C spectroscopy was then conducted to confirm the presence of different C atoms in the COFs. The solid-state <sup>13</sup>C spectrum of H-COF showed a peak at 156 ppm attributable to the C=N linkage (Fig. 3C, black curve), peaks from PYTA at 150.9–122.5 ppm, and a peak at 129.1 ppm due to the TP units. Upon

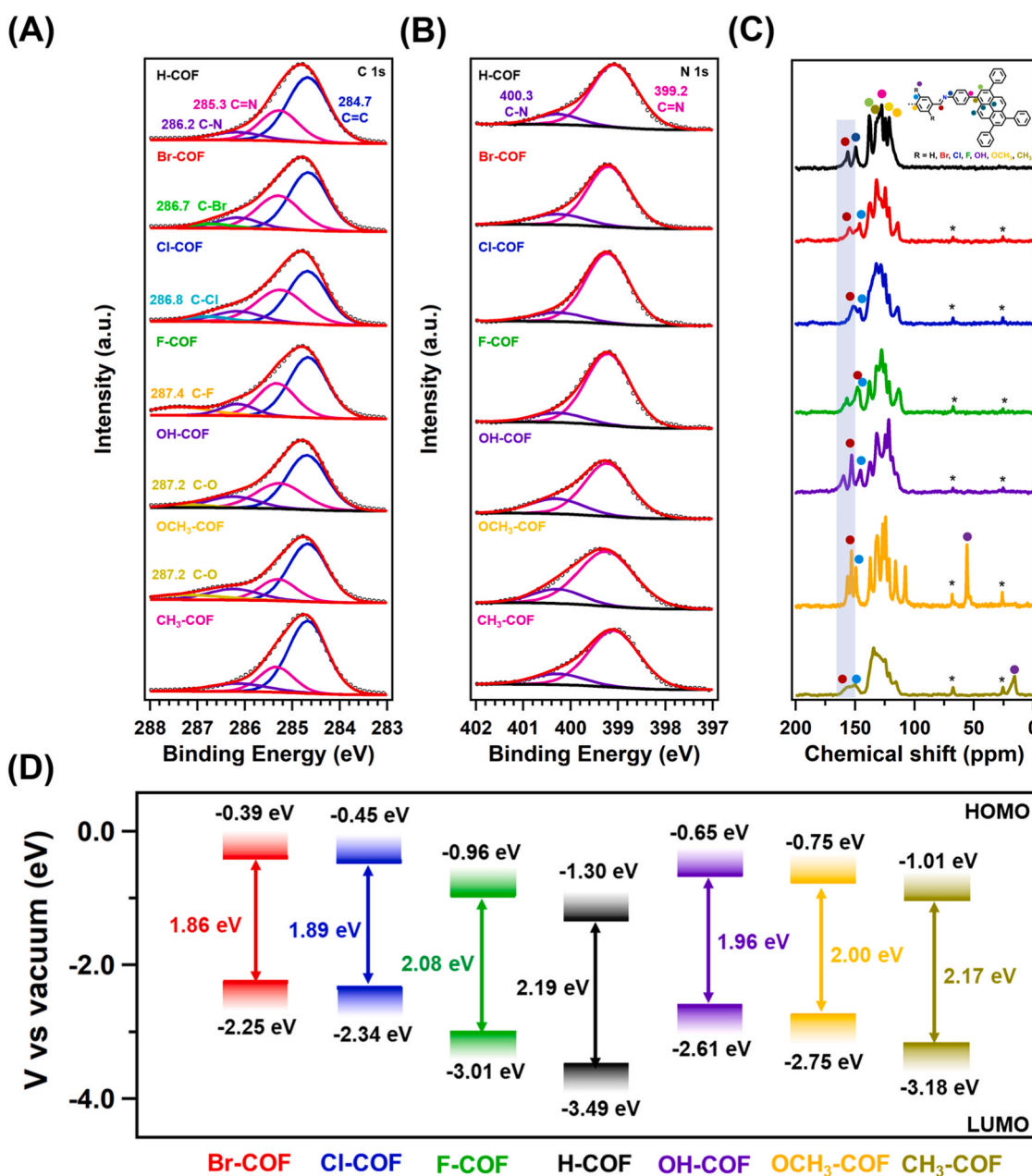


**Fig. 3.** High-resolution XPS spectra of (A) C 1s and (B) N 1s high-resolution X-ray photoelectron spectroscopy (XPS) spectra of R-COFs, (C) <sup>13</sup>C CP/MAS spectra, asterisks denote THF and (D) lowest unoccupied molecular orbital (LUMO) and highest occupied molecular orbital (HOMO) levels of H-COF (black curve), Br-COF (red curve), Cl-COF (blue curve), F-COF (green curve), OH-COF (purple curve), OCH<sub>3</sub>-COF (orange curve), and CH<sub>3</sub>-COF (yellow curve).

introducing electron-withdrawing groups in the linkers, the peaks of the C=N linkages were slightly high-field-shifted to 154.8, 151.7, 149.4 ppm for Br-COF, Cl-COF, and F-COF, respectively. Moreover, the peaks from the C-Br, C-Cl, and C-F bonds appeared at 123.1, 130.0, and 157.2 ppm, respectively. In contrast, the introduction of electron-donating groups in the COFs resulted in low-field shifts of the peaks of the C=N bonds, which appeared at 149.4, 152.9, and 157.7 ppm for OH-COF, OCH<sub>3</sub>-COF, and CH<sub>3</sub>-COF, respectively. The peaks due to C-OH, C-OCH<sub>3</sub>, and C-CH<sub>3</sub> bonds were observed at 148.8, 151.0, and 133.9 ppm, with the signals of OCH<sub>3</sub> and CH<sub>3</sub> appearing at 56.0 and 15.6 ppm, respectively. [56] In addition, all the C atoms in the skeletons were clearly identified in the spectra of all the COFs. Taken together, these results suggest that the introduction of the electron-withdrawing groups strengthens the interaction between adjacent COF layers, increasing the electron density that surrounds and shields the C nuclei of the C=N linkages and thus shifting the NMR signals toward the high-field region, whereas the opposite is true for the electron-donating groups [57].

To explore the influence of the linkers on the electronic states of the COFs, their electron transfer abilities were studied using ultraviolet-visible (UV-vis) absorption spectroscopy. H-COF showed bands in the absorption range of 200–800 nm (Fig. S17, black curve), and the corresponding optical bandgap calculated using the Tauc plots was 2.19 eV. (Fig. S18A). Introducing different functional groups promoted the electronic transfer ability along the frameworks, affording bandgaps of 1.86, 1.89, 1.96, 2.00, 2.08, and 2.17 eV for Br-COF, Cl-COF, OH-COF, OCH<sub>3</sub>-COF, F-COF, and CH<sub>3</sub>-COF, respectively (Fig. S18B-G). Moreover, the electron transfer states in the frameworks were further investigated by performing Mott-Schottky measurements to determine the lowest unoccupied molecular orbital (LUMO) and highest occupied molecular orbital (HOMO) positions (Fig. S19). The HOMO positions of Br-COF, Cl-COF, F-COF, OH-COF, OCH<sub>3</sub>-COF, CH<sub>3</sub>-COF, and H-COF were calculated to be -0.39 eV, -0.45 eV, -0.96 eV, -0.65 eV, -0.75 eV, -1.01 eV and -1.30 eV, respectively, via UV-vis and Mott-Schottky measurements (Fig. 3D). Importantly, Br-COF exhibited the highest HOMO level among all the synthesized COFs, indicating its strongest reductive ability. [58,59].

In addition to the reductive ability, the dipole moments and the O<sub>2</sub> binding ability of the COFs were explored. The dipole moments of H-COF, F-COF, Cl-COF, Br-COF, OH-COF, OCH<sub>3</sub>-COF and CH<sub>3</sub>-COF were determined to be 1.47, 1.19, 1.29, 1.27, 1.36, 4.24, and 1.56 Debye, respectively, proving the existence of the intermolecular polarization thus promoted charge-redistribution in the molecular backbones, which may be conducive to the catalytic activity towards ORR (Fig. 4A-G). [60–63] The binding ability of O<sub>2</sub> on the COFs were then studied. To investigate the O<sub>2</sub> binding ability of the COFs, the HOMO and LUMO distributions were calculated, and the possible O<sub>2</sub> binding sites were obtained according to the LUMO distributions. The binding energies (*E*<sub>ads</sub>) for site 1, 2, and 3 of H-COF were estimated to be -0.41, -0.45, -0.28 eV, respectively (Fig. 4H and Fig. S20). The *E*<sub>ads</sub> values of Br-COF, Cl-COF, F-COF, OH-COF, OCH<sub>3</sub>-COF, CH<sub>3</sub>-COF, and H-COF were -0.43, -0.43, -0.51, -0.55, -0.53, -0.54, and -0.45 eV, respectively (Fig. 4I-N). Thus, all the COFs showed similar O<sub>2</sub> binding ability. (Fig. S21-26).

The contact angle plays an important role in the three-phase interface between an ORR catalyst and a gas diffusion electrode (Fig. S27). All the COFs displayed hydrophobic features, with the water contact angle of Br-COF, Cl-COF, OH-COF, OCH<sub>3</sub>-COF, F-COF, CH<sub>3</sub>-COF, and H-COF being 138°, 137°, 128°, 128°, 139°, 128°, and 136°, respectively, thus facilitating the diffusion of O<sub>2</sub> to the active sites and maintaining the stability of the electrode.

The thermal stability and chemical stability of all the COFs were investigated. A thermogravimetric analysis revealed that the COFs were thermally stable up to 300 °C under N<sub>2</sub> atmosphere (Fig. S28). In addition, their crystallinity was retained after treatment with a 0.1 M KOH solution for seven days (Fig. S29), indicating the stability of their

ordered frameworks.

### 3.2. Electrocatalytic performance of COFs

Next, the electronic catalytic performance of the COFs was investigated by conducting cyclic voltammetry (CV) measurements in N<sub>2</sub>- or O<sub>2</sub>-saturated 0.1 M KOH aqueous solutions. Reductive peaks were observed for all the COFs under O<sub>2</sub> atmosphere, whereas no peaks were identified in N<sub>2</sub>-saturated solutions, indicating their catalytic activity toward ORR (Fig. S30). The catalytic behavior of the COFs was then evaluated via rotating ring disk electrode (RRDE) measurements. The current densities obtained from the disk and ring electrodes reflected the activity for the total ORR and 2e<sup>-</sup> activities. Using the corresponding linear sweep voltammetry (LSV) curve of H-COF, the onset potential (*E*<sub>o</sub>) at a current density of 0.1 mA cm<sup>-2</sup> was determined to be 0.67 V, the half-wave potential (*E*<sub>1/2</sub>) was 0.60 V, and the limited current density (*J*<sub>lim</sub>) at 0.2 V was 1.60 mA cm<sup>-2</sup>. (Fig. 5A, black curve). Meanwhile, Br-COF, Cl-COF, F-COF, OH-COF, OCH<sub>3</sub>-COF, and CH<sub>3</sub>-COF showed *E*<sub>o</sub> values of 0.70, 0.67, 0.67, 0.66, 0.66, and 0.66 V and *E*<sub>1/2</sub> values of 0.61, 0.60, 0.60, 0.57, 0.59, and 0.60 V, respectively. The COFs with electron-withdrawing groups exhibited current densities higher than those with electron-donating groups, with the *J*<sub>lim</sub> values of Br-COF, Cl-COF, and F-COF being 2.34, 2.02, and 1.99 mA cm<sup>-2</sup> and those of OH-COF, OCH<sub>3</sub>-COF, and CH<sub>3</sub>-COF being 1.98, 1.67, and 1.60 mA cm<sup>-2</sup>, respectively (Fig. 5A).

The Tafel slopes of the catalysts were determined using the LSV curves. H-COF showed a Tafel slope of 96 mV dec<sup>-1</sup>, while those of Br-COF, Cl-COF, F-COF, OH-COF, OCH<sub>3</sub>-COF, and CH<sub>3</sub>-COF were 70, 80, 91, 83, 89, and 93 mV dec<sup>-1</sup>, respectively (Fig. 5B), suggesting the faster kinetic behavior of the substituted COFs. In particular, Br-COF exhibited the smallest Tafel slope, which revealed that the Br substituents in the frameworks enhanced the kinetic transfer behavior.

In addition, the mass activity and TOF values were calculated at a potential of 0.5 V. Br-COF showed the highest TOF value of 0.2498 s<sup>-1</sup> with a mass activity of 32.0 A g<sup>-1</sup>, which were 2.32 and 1.75 times higher than those H-COF, respectively. The TOF and mass activity values of F-COF and Cl-COF were 0.1535 and 0.1787 s<sup>-1</sup> and 27.0 and 24.9 A g<sup>-1</sup>, respectively (Fig. 5C). The COFs with electron-donating groups exhibited similar TOF and mass activity values; the TOF values of OH-COF, OCH<sub>3</sub>-COF, and CH<sub>3</sub>-COF were 0.1360, 0.1310, and 0.1336 s<sup>-1</sup>, respectively, and their mass activity values were 25.3, 21.2, and 20.6 A g<sup>-1</sup>, respectively.

In addition to the total activity, the current densities obtained from the RRDE measurements revealed that the electron-withdrawing substituents contributed to achieve higher 2e<sup>-</sup>-ORR activity. Thus, the ring current densities were determined to be 0.86, 0.72, 0.67, 0.68, 0.57, 0.67, and 0.49 mA cm<sup>-2</sup> at 0.2 V for Br-COF, Cl-COF, F-COF, OH-COF, OCH<sub>3</sub>-COF, CH<sub>3</sub>-COF, and H-COF, respectively, suggesting that the catalytic activity decrease in the order Br-COF > Cl-COF > OH-COF > F-COF > CH<sub>3</sub>-COF > OCH<sub>3</sub>-COF > H-COF. The catalytic selectivity was also investigated for all the COFs. H-COF achieved a H<sub>2</sub>O<sub>2</sub> selectivity from 76.9% to 73.3% at a potential range of 0.2–0.6 V (Fig. 5D, black curve). Meanwhile, the H<sub>2</sub>O<sub>2</sub> selectivity was clearly enhanced upon introducing the Br, Cl, and F substituents in the linkers, reaching maximum values of 85.4–85.5% (Fig. 5D, red curve), 84.4–82.4% (Fig. 5D, blue curve), and 81.2–78.1% (Fig. 5D, green curve) for Br-COF, Cl-COF, F-COF, respectively. For the COFs bearing electron-donating substituents, the H<sub>2</sub>O<sub>2</sub> selectivity was similar or slightly lower (82.3%–79.7%, 81.9%–80.1%, and 82.6%–78.8% for OH-COF, OCH<sub>3</sub>-COF, and CH<sub>3</sub>-COF, respectively, at a potential range of 0.2–0.6 V). According to the RRDE measurements, the electron transfer number (*n*) values for all the synthesized COFs were obtained (Fig. 5E). The *n* values for H-COF ranged from 2.53 to 2.46 at a potential range of 0.2–0.6 V, indicating that H-COF catalyzed the ORR via a mixed 2e<sup>-</sup>/4e<sup>-</sup> pathway, whereas an obvious decline in the *n* values was observed upon substitution. Br-COF showed the smallest *n* values of 2.29–2.26 at the same

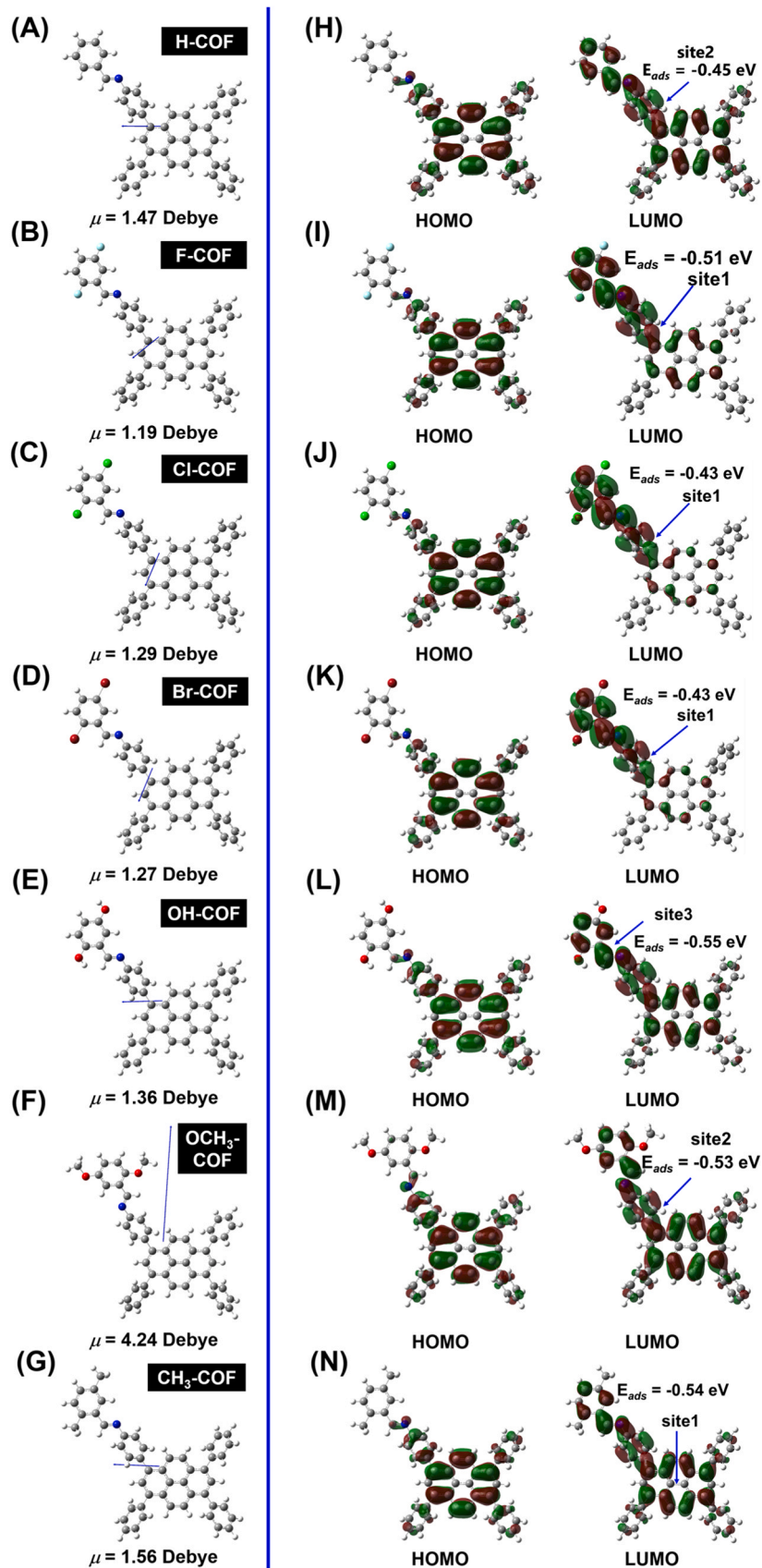


**Fig. 4.** Dipole moments for (A) H-COF, (B) F-COF, (C) Cl-COF, (D) Br-COF, (E) OH-COF, (F) OCH<sub>3</sub>-COF, and (G) CH<sub>3</sub>-COF. The binding ability of the  $O_2$  for (H) H-COF, (I) F-COF, (J) Cl-COF, (K) Br-COF, (L) OH-COF, (M) OCH<sub>3</sub>-COF, and (N) CH<sub>3</sub>-COF.

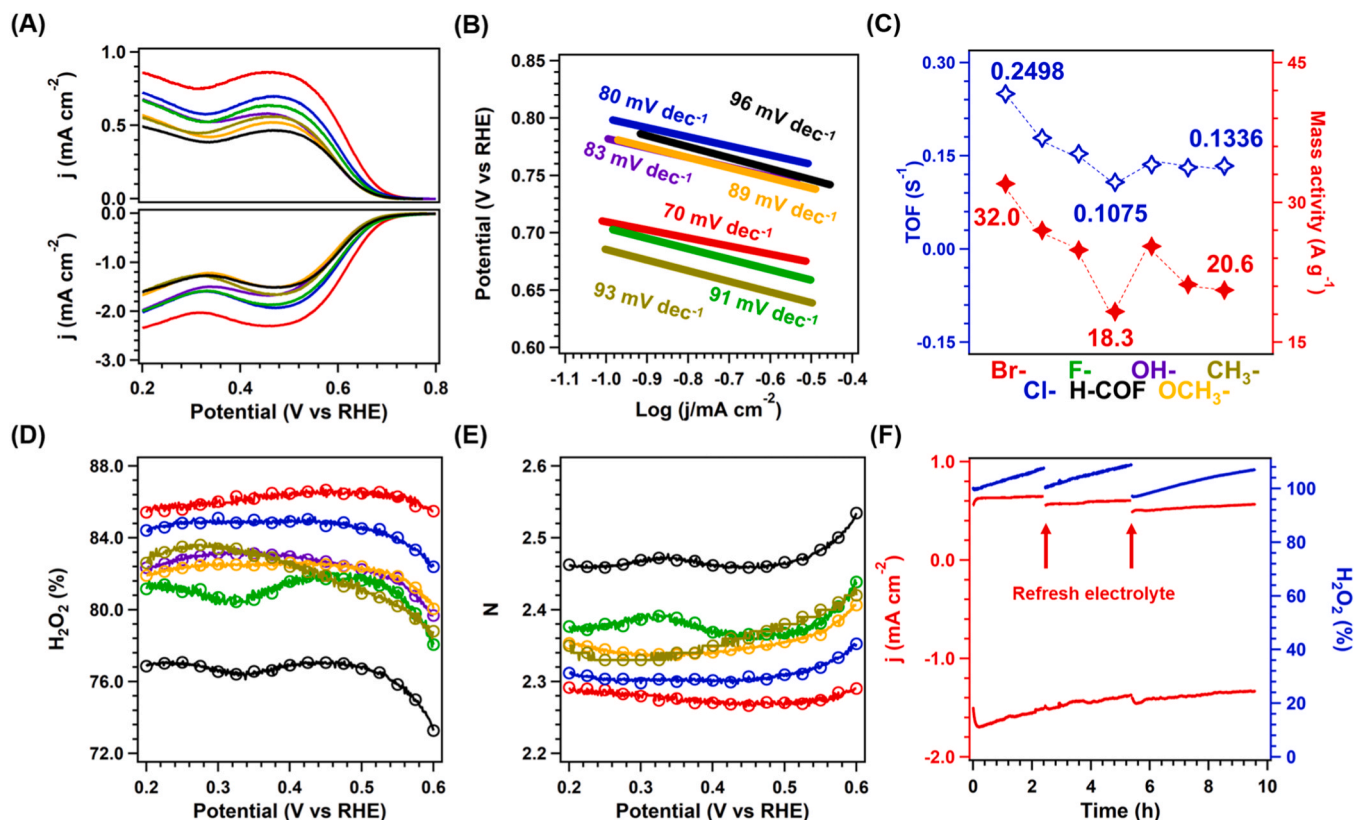


**Fig. 5.** (A) LSV curves, (B) Tafel slopes, (C) comparison of the TOFs and mass activities, and (D) electron transfer number, and (E) H<sub>2</sub>O<sub>2</sub> yield plots determined via the RRDE measurements for F-COF (green curves), Cl-COF (blue curves), Br-COF (red curves), H-COF (black curves), OH-COF (purple curves), OCH<sub>3</sub>-COF (orange curves) and CH<sub>3</sub>-COF (yellow curves) in O<sub>2</sub>-saturated KOH (0.1 M) aqueous solution. (F) Long-term stability of Br-COF at 0.3 V for 10 h.

potential range, suggesting that its selectivity was the highest.

The long-term stability of COFs as 2e<sup>-</sup>-ORR catalysts is a serious issue. Therefore, Br-COF was investigated for 10 h at a potential of 0.3 V. The initial current density was  $-1.5 \text{ mA cm}^{-2}$  and the selectivity was 107% after 3 h (Fig. 5F). The FT IR spectra (Fig. S31) and PXRD patterns (Fig. S32) for catalytic Br-COF were obtained after long-term stability. After the long-term stability test, Br-COF was subjected to FT-IR spectroscopy and PXRD analyses, finding that all the peaks were retained, which demonstrated the good long-term stability of Br-COF. Using iodometric titration, the Faradaic efficiency of Br-COF for H<sub>2</sub>O<sub>2</sub> production was determined to be 80.6% at a potential of 0.3 V (Fig. S33).

To better understand their different catalytic activity, we obtained the electrochemical active surface area (ECSA) by the electrochemical double layer capacitances ( $C_{dl}$ ) with using the CV measurement at the different scan rates (Fig. S34). Correspondingly, the  $C_{dl}$  values for the Br<sup>-</sup>, Cl<sup>-</sup>, F<sup>-</sup>, H<sup>+</sup>, OH<sup>-</sup>, OCH<sub>3</sub><sup>-</sup> and CH<sub>3</sub>-COF were 2.95, 3.62, 3.20, 3.20, 3.50, 4.20 and 2.37 mF cm<sup>-2</sup>, respectively (Fig. S35). The LSV curves were then normalized by the ECSA. Accordingly, Within the potential range of 0.2 to 0.8 V, the Br-COFs always exhibited the higher normalized current density than that of H-COF, confirming that introducing the Br substituent in the linkers helped to improve the COF activity towards ORR (Figs. S36). Electrochemical impedance spectroscopy measurements were also performed. As shown in Fig. S37, the Nyquist curves of Br-COF showed a smaller semicircular diameter than those of H-COF, indicating that the introduction of a substituent could reduce the resistance of the materials, improve the electronic conductivity, and enhance the charge transfer.

### 3.3. Theoretical calculations

Considering the different electronic states of the COFs, we tried to

identify the properties that contributed to the catalytic activity. The relationship between the catalytic activity (determined as the current density at 0.2 V), the reductive ability (HOMO level), the polarity (dipole moments), and the O<sub>2</sub> binding ability (binding energy) are summarized in Fig. 6A-D. Accordingly, the change in current density was related to the HOMO level, whereas it differed from the dipole moments and the O<sub>2</sub> binding energy. Thus, the catalytic activity mainly depends on the reductive ability of the COFs. Moreover, to gain more insight into the catalytic mechanism of the ORR catalyzed by the COFs, DFT calculations were conducted. First, a Bader charge analysis was performed for the atoms in the COFs to determine the most favorable catalytic sites, finding that the C atoms displayed more negative charges than other atoms in the COFs, which suggested that the catalytic sites in all the COFs were the C atoms in the linkages (Fig. S38-44). Moreover, the free-energy changes ( $\Delta G$ ) in the catalytic process on the carbon atoms in the linkages were calculated at an applied potential of 0.7 V (Fig. 6E and F). The obtained  $\Delta G$  values followed the sequence Br-COF (0.970 eV) < Cl-COF (0.981 eV) < F-COF (1.006 eV) < OH-COF (1.237 eV) < OCH<sub>3</sub>-COF (1.278 eV) < H-COF (1.345 eV) < CH<sub>3</sub>-COF (1.372 eV), which is in accord with the experimental results. In addition, the  $\Delta G$  was calculated for the 4e<sup>-</sup>-ORR process catalyzed by Br-COF at a potential of 1.23 V (Fig. S45). The rate-determining step was the formation of an OOH\* intermediate with a  $\Delta G$  of 1.50 eV. In addition, the  $\Delta G$  from O\* to OH\* was 0.26 eV > 0 eV, confirming that the 4e<sup>-</sup> pathway was unfavored. Thus, the 2e<sup>-</sup> pathway is the most probable route for the ORR catalyzed by Br-COF.

## 4. Conclusions

We explored the specific effects among the electronic features of COFs that determine their electrocatalytic activity for the 2e<sup>-</sup> ORR. By using a linker engineering strategy, seven COFs with similar topologies

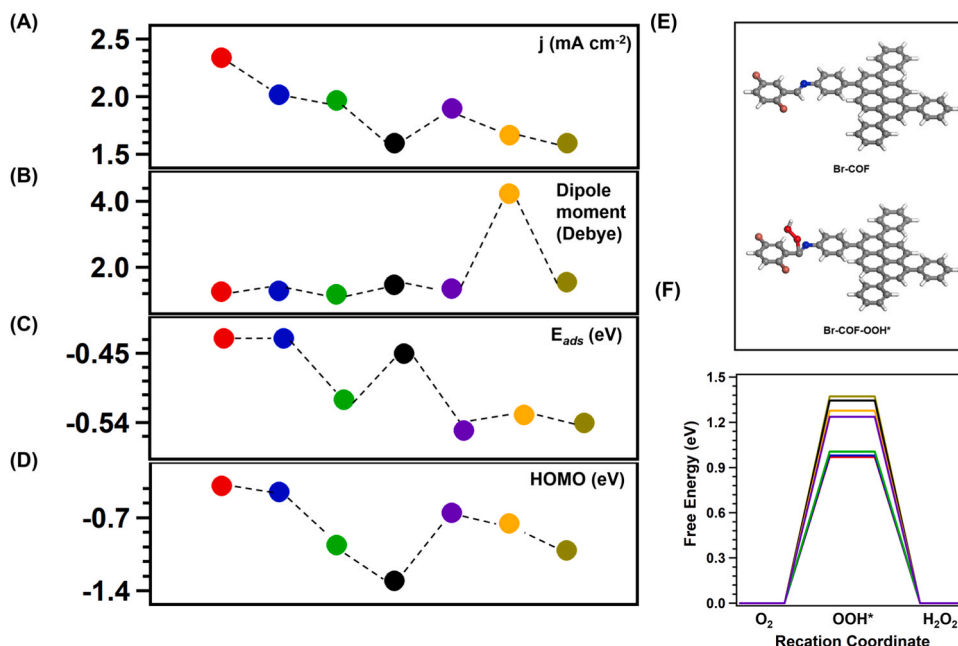


**Fig. 6.** (A) Activity, (B) dipole moment, (C) O<sub>2</sub> adsorption energy, (D) HOMO levels for H-COF (black curve), Br-COF (red curves), Cl-COF (blue curves), F-COF (green curves), OH-COF (purple curves), OCH<sub>3</sub>-COF (orange curves), and CH<sub>3</sub>-COF (yellow curves). (E) The schematic mechanism for ORR of COFs. (F) The relative energy diagram of 2e<sup>-</sup> pathway of ORR for H-COF (black curve), Br-COF (red curves), Cl-COF (blue curves), F-COF (green curves), OH-COF (purple curves), OCH<sub>3</sub>-COF (orange curves), and CH<sub>3</sub>-COF (yellow curves) at 0.7 V.

and pore size/shapes, ordered skeletons, and O<sub>2</sub> binding ability but possessing different bandgaps and polarity were successfully prepared to investigate the reasons for their different catalytic performance. The COF bearing Br atoms in the linkers exhibited the highest activity and selectivity in the 2e<sup>-</sup> ORR, affording TOF and mass activity values that were 2.32 and 1.75 times higher than those of H-COF without substituents. The experimental and theoretical results revealed that the activity mainly depends on the reductive ability of the COFs, leading to different ability to form intermediates. This work provides a new guidance for the design of highly active ORR catalysts.

### Declaration of Competing Interest

The authors declare that they have no known competing financial interests or personal relationships that could have appeared to influence the work reported in this paper.

### Data Availability

Data will be made available on request.

### Acknowledgements

The authors acknowledge the financial support from the National key research and development program (2022YFA1503801), the Natural Science Foundation of Shanghai (20ZR1464000 and 22ZR1470100), the National Natural Science Foundation of China (22075309 and 52303288), the Youth Innovation Promotion Association of Chinese Academy of Sciences. (E324441401) The authors would like to thank Suzhou Deyo Bot Advanced Materials Co., Ltd. ([www.dy-test.com](http://www.dy-test.com)) for providing support on material characterization.

### Appendix A. Supporting information

Supplementary data associated with this article can be found in the online version at [doi:10.1016/j.apcatb.2023.123611](https://doi.org/10.1016/j.apcatb.2023.123611).

### References

- [1] C.S. Diercks, O.M. Yaghi, The atom, the molecule, and the covalent organic framework, *Science* 355 (2017) 6328.
- [2] X. Li, K. Zhang, G. Wang, Y. Yuan, G. Zhan, T. Ghosh, W.P.D. Wong, F. Chen, H.-S. Xu, U. Mirsaidov, K. Xie, J. Lin, K.P. Loh, Constructing ambivalent imidazopyridinium-linked covalent organic frameworks, *Nat. Synth.* 1 (2022) 382–392.
- [3] X. Liu, L. Dai, Carbon-based metal-free catalysts, *Nat. Rev. Mater.* 1 (2016), 16064.
- [4] C. Qian, L. Feng, W.L. Teo, J. Liu, W. Zhou, D. Wang, Y. Zhao, Imine and imine-derived linkages in two-dimensional covalent organic frameworks, *Nat. Rev. Chem.* 6 (2022) 881–898.
- [5] K. Wang, Z. Jia, Y. Bai, X. Wang, S.E. Hodgkiss, L. Chen, S.Y. Chong, X. Wang, H. Yang, Y. Xu, F. Feng, J.W. Ward, A.I. Cooper, Synthesis of stable thiazole-linked covalent organic frameworks via a multicomponent reaction, *J. Am. Chem. Soc.* 142 (2020) 11131–11138.
- [6] A. Acharjya, L. Longworth-Dunbar, J. Roeser, P. Pachfule, A. Thomas, Synthesis of vinylene-linked covalent organic frameworks from acetonitrile: combining cyclotrimerization and aldol condensation in one pot, *J. Am. Chem. Soc.* 142 (2020) 14033–14038.
- [7] S. Bi, C. Yang, W. Zhang, J. Xu, L. Liu, D. Wu, X. Wang, Y. Han, Q. Liang, F. Zhang, Two-dimensional semiconducting covalent organic frameworks via condensation at arylmethyl carbon atoms, *Nat. Commun.* 10 (2019) 2467.
- [8] K. Xiong, Y. Wang, F. Zhang, X. Li, X. Lang, Linker length-dependent photocatalytic activity of  $\beta$ -ketonamine covalent organic frameworks, *Appl. Catal. B: Environ.* 322 (2023), 122135.
- [9] J. Li, X. Jing, Q. Li, S. Li, X. Gao, X. Feng, B. Wang, Bulk COFs and COF nanosheets for electrochemical energy storage and conversion, *Chem. Soc. Rev.* 49 (2020) 3565–3604.
- [10] M. Traxler, S. Gisbertz, P. Pachfule, J. Schmidt, J. Roeser, S. Reischauer, J. Rabeah, B. Pieber, A. Thomas, Acridine-functionalized covalent organic frameworks (COFs) as photocatalysts for metallaphotocatalytic C–N cross-coupling, *Angew. Chem. Int. Ed.* 61 (2022), e202117738.
- [11] Y.K. Im, D.G. Lee, H.J. Noh, S.Y. Yu, J. Mahmood, S.Y. Lee, J.B. Baek, Crystalline porphyrazine-linked fused aromatic networks with high proton conductivity, *Angew. Chem. Int. Ed.* 61 (2022), e202203250.
- [12] C. Kang, Z. Zhang, S. Kusaka, K. Negita, A.K. Usadi, D.C. Calabro, L.S. Baugh, Y. Wang, X. Zou, Z. Huang, R. Matsuda, D. Zhao, Covalent organic framework atropisomers with multiple gas-triggered structural flexibilities, *Nat. Mater.* 22 (2023) 636–643.
- [13] Y. Li, L. Guo, Y. Lv, Z. Zhao, Y. Ma, W. Chen, G. Xing, D. Jiang, L. Chen, Polymorphism of 2D imine covalent organic frameworks, *Angew. Chem. Int. Ed.* 60 (2021) 5363–5369.
- [14] Y. Su, Z. Chen, X. Tang, H. Xu, Y. Zhang, C. Gu, Design of persistent and stable porous radical polymers by electronic isolation strategy, *Angew. Chem. Int. Ed.* 60 (2021) 24424–24429.

- [15] S.S. Zhao, J. Liang, D.-H. Si, M.-J. Mao, Y.B. Huang, R. Cao, Superheterojunction covalent organic frameworks: Supramolecular synergetic charge transfer for highly efficient photocatalytic CO<sub>2</sub> reduction, *Appl. Catal. B* 333 (2023), 122782.
- [16] Q. An, L. Wang, G. Zhao, L. Duan, Y. Sun, Q. Liu, Z. Mei, Y. Yang, C. Zhang, H. Guo, Constructing cooperative interface via Bi-functional COF for facilitating the sulfur conversion and Li(+) dynamics, *Adv. Mater.* (2023), e2305818.
- [17] S. Yang, X. Li, T. Tan, J. Mao, Q. Xu, M. Liu, Q. Miao, B. Mei, P. Qiao, S. Gu, F. Sun, J. Ma, G. Zeng, Z. Jiang, A fully-conjugated covalent organic framework-derived carbon supporting ultra-close single atom sites for ORR, *Appl. Catal. B* 307 (2022), 121147.
- [18] M. Liu, H.Y. Kong, S. Bi, X. Ding, G.Z. Chen, J. He, Q. Xu, B.H. Han, G. Zeng, Non-interpenetrated 3D covalent organic framework with dia topology for Au ions capture, *Adv. Funct. Mater.* 33 (2023) 2302637.
- [19] S. Huang, B. Zhang, D. Wu, Y. Xu, H. Hu, F. Duan, H. Zhu, M. Du, S. Lu, Linkage engineering in covalent organic frameworks as metal-free oxygen reduction electrocatalysts for hydrogen peroxide production, *Appl. Catal. B* 340 (2024), 123216.
- [20] J.Y. Yue, L.P. Song, Y.F. Fan, Z.X. Pan, P. Yang, Y. Ma, Q. Xu, B. Tang, Thiophene-containing covalent organic frameworks for overall photocatalytic H<sub>2</sub>(O)<sub>2</sub> synthesis in water and seawater, *Angew. Chem. Int. Ed.* (2023) e202309624.
- [21] S. Yang, Q. Cheng, J. Mao, Q. Xu, Y. Zhang, Y. Guo, T. Tan, W. Luo, H. Yang, Z. Jiang, Rational design of edges of covalent organic networks for catalyzing hydrogen peroxide production, *Appl. Catal. B* 298 (2021), 120605.
- [22] D. Li, C. Li, L. Zhang, H. Li, L. Zhu, D. Yang, Q. Fang, S. Qiu, X. Yao, Metal-free thiophene-sulfur covalent organic frameworks: precise and controllable synthesis of catalytic active sites for oxygen reduction, *J. Am. Chem. Soc.* 142 (2020) 8104–8108.
- [23] X. Li, S. Yang, M. Liu, X. Yang, Q. Xu, G. Zeng, Z. Jiang, Catalytic linkage engineering of covalent organic frameworks for the oxygen reduction reaction, *Angew. Chem. Int. Ed.* 62 (2023), e202304356.
- [24] Q. Miao, Z. Chen, X. Li, M. Liu, G. Liu, X. Yang, Z. Guo, C. Yu, Q. Xu, G. Zeng, Construction of catalytic Fe<sub>2</sub>N<sub>2</sub>S sites in covalent organic framework-derived carbon for catalyzing the oxygen reduction reaction, *Acs. Catal.* 13 (2023) 11127–11135.
- [25] Y. Wang, F. Huang, W. Sheng, X. Miao, X. Li, X.-K. Gu, X. Lang, Blue light photocatalytic oxidation of sulfides to sulfoxides with oxygen over a thiazole-linked 2D covalent organic framework, *Appl. Catal. B* 338 (2023), 123070.
- [26] X. Yang, X. Li, M. Liu, S. Yang, Q. Niu, L. Zhai, Z. Jiang, Q. Xu, G. Zeng, Modulating electrochemical CO<sub>2</sub> reduction performance via sulfur-containing linkages engineering in metallophthalocyanine based covalent organic frameworks, *Acs. Mater. Lett.* 5 (2023) 1611–1618.
- [27] E. Luo, Y. Chu, J. Liu, Z. Shi, S. Zhu, L. Gong, J. Ge, C.H. Choi, C. Liu, W. Xing, Pyrolyzed M-Nx catalysts for oxygen reduction reaction: progress and prospects, *Energy Environ. Sci.* 14 (2021) 2158–2185.
- [28] M. Yan, Z. Wei, Z. Gong, B. Johannessen, G. Ye, G. He, J. Liu, S. Zhao, C. Cui, H. Fei, Sb<sub>2</sub>S<sub>3</sub>-templated synthesis of sulfur-doped Sb-N-C with hierarchical architecture and high metal loading for H<sub>2</sub>O<sub>2</sub> electrosynthesis, *Nat. Commun.* 14 (2023).
- [29] X. Li, S. Yang, M. Liu, S. Liu, Q. Miao, Z. Duan, P. Qiao, J. Lin, F. Sun, Q. Xu, Z. Jiang, Immobilization of platinum nanoparticles on covalent organic framework-derived carbon for oxygen reduction catalysis, *Small Struct.* 4 (2023) 2200320.
- [30] Z. Zhou, M. Sun, Y. Zhu, P. Li, Y. Zhang, M. Wang, Y. Shen, A thioether-decorated triazine-based covalent organic framework towards overall H<sub>2</sub>O<sub>2</sub> photosynthesis without sacrificial agents, *Appl. Catal. B* 334 (2023), 122862.
- [31] X. Yan, B. Wang, J. Ren, X. Long, D. Yang, An unsaturated bond strategy to regulate active centers of metal-free covalent organic frameworks for efficient oxygen reduction, *Angew. Chem. Int. Ed.* 61 (2022) e202209583.
- [32] S. Yang, L. Lu, J. Li, Q. Cheng, B. Mei, X. Li, J. Mao, P. Qiao, F. Sun, J. Ma, Q. Xu, Z. Jiang, Boosting hydrogen peroxide production via establishment and reconstruction of single-metal sites in covalent organic frameworks, *SusMat* 3 (2023) 379–389.
- [33] Z. You, B. Wang, Z. Zhao, Q. Zhang, W. Song, C. Zhang, X. Long, Y. Xia, Metal-free carbon-based covalent organic frameworks with heteroatom-free units boost efficient oxygen reduction, *Adv. Mater.* 35 (2023) e2209129.
- [34] L. Zhai, S. Yang, X. Yang, W. Ye, J. Wang, W. Chen, Y. Guo, L. Mi, Z. Wu, C. Soutis, Q. Xu, Z. Jiang, Conjugated covalent organic frameworks as platinum nanoparticle supports for catalyzing the oxygen reduction reaction, *Chem. Mater.* 32 (2020) 9747–9752.
- [35] S. Huang, B. Zhang, H. Sun, H. Hu, J. Wang, F. Duan, H. Zhu, M. Du, S. Lu, Constructing single atom sites on bipyridine covalent organic frameworks for selective electrochemical production of H<sub>2</sub>O<sub>2</sub>, *Chem. Commun.* 59 (2023) 10424–10427.
- [36] Z. Wu, J. Luo, Y. Liang, X. Yu, Y. Zhao, Y. Li, W. Wang, Z. Sui, X. Tian, Q. Chen, Tetrazole-functionalized benzoquinoline-linked covalent organic frameworks with efficient performance for electrocatalytic H<sub>2</sub>O<sub>2</sub> production and Li-S batteries, *Mater. Chem. Front.* 7 (2023) 1650–1658.
- [37] C. Liu, H. Li, F. Liu, J. Chen, Z. Yu, Z. Yuan, C. Wang, H. Zheng, G. Henkelman, L. Wei, Y. Chen, Intrinsic activity of metal centers in metal-nitrogen-carbon single-atom catalysts for hydrogen peroxide synthesis, *J. Am. Chem. Soc.* 142 (2020) 21861–21871.
- [38] M. Liu, S. Yang, S. Liu, Q. Miao, X. Yang, X. Li, Q. Xu, G. Zeng, Construction of atomic Metal-N<sub>2</sub> sites by interlayers of covalent organic frameworks for electrochemical H<sub>2</sub>O<sub>2</sub> synthesis, *Small* 18 (2022) 2204757.
- [39] S. Huang, S. Lu, Y. Hu, Y. Cao, Y. Li, F. Duan, H. Zhu, Y. Jin, M. Du, W. Zhang, Covalent organic frameworks with molecular electronic modulation as metal-free electrocatalysts for efficient hydrogen peroxide production, *Small Struct.* 4 (2023) 2200387.
- [40] S. Huang, B. Zhang, D. Wu, Y. Xu, H. Hu, F. Duan, H. Zhu, M. Du, S. Lu, Linkage engineering in covalent organic frameworks as metal-free oxygen reduction electrocatalysts for hydrogen peroxide production, *Appl. Catal. B* 340 (2024), 123216.
- [41] X. Xu, Y. Gao, Q. Yang, T. Liang, B. Luo, D. Kong, X. Li, L. Zhi, B. Wang, Regulating the activity of intrinsic sites in covalent organic frameworks by introducing electro-withdrawing groups towards highly selective H<sub>2</sub>O<sub>2</sub> electrosynthesis, *Nano Today* 49 (2023), 101792.
- [42] J.-N. Chang, Q. Li, J.-W. Shi, M. Zhang, L. Zhang, S. Li, Y. Chen, S.-L. Li, Y.-Q. Lan, Oxidation-reduction molecular junction covalent organic frameworks for full reaction photosynthesis of H<sub>2</sub>O<sub>2</sub>, *Angew. Chem. Int. Ed.* 62 (2023), e202218868.
- [43] L. Zhai, Z. Xie, C.-X. Cui, X. Yang, Q. Xu, X. Ke, M. Liu, L.-B. Qu, X. Chen, L. Mi, Constructing synergistic triazine and acetylene cores in fully conjugated covalent organic frameworks for cascade photocatalytic H<sub>2</sub>O<sub>2</sub> production, *Chem. Mater.* 34 (2022) 5232–5240.
- [44] Y. Zhang, Z. Qiao, R. Zhang, Z. Wang, H.J. Wang, J. Zhao, D. Cao, S. Wang, Multicomponent synthesis of imidazole-linked fully conjugated 3d covalent organic framework for efficient electrochemical hydrogen peroxide production, *Angew. Chem. Int. Ed.* (2023), e202314539.
- [45] M. Martínez-Fernández, E. Martínez-Periñán, A. de la Peña Ruigómez, J.J. Cabrera-Trujillo, J.A.R. Navarro, F. Aguilar-Galindo, D. Rodríguez-San-Miguel, M. Ramos, R. Vismara, F. Zamora, E. Lorenzo, J.L. Segura, Scalable synthesis and electrocatalytic performance of highly fluorinated covalent organic frameworks for oxygen reduction, *Angew. Chem. Int. Ed.* 62 (2023), e202313940.
- [46] J.P. Jeon, Y.J. Kim, S.H. Joo, H.J. Noh, S.K. Kwak, J.B. Baek, Benzotrithiophene-based covalent organic framework photocatalysts with controlled conjugation of building blocks for charge stabilization, *Angew. Chem. Int. Ed.* 62 (2023), e202217416.
- [47] X. Zhao, P. Pachfule, A. Thomas, Covalent organic frameworks (COFs) for electrochemical applications, *Chem. Soc. Rev.* 50 (2021) 6871–6913.
- [48] S. An, X. Li, S. Shang, T. Xu, S. Yang, C.X. Cui, C. Peng, H. Liu, Q. Xu, Z. Jiang, J. Hu, One-dimensional covalent organic frameworks for the 2e(-) oxygen reduction reaction, *Angew. Chem. Int. Ed.* 62 (2023), e202218742.
- [49] Y. Liu, H. Tan, Y. Wei, M. Liu, J. Hong, W. Gao, S. Zhao, S. Zhang, S. Guo, Cu(2)O/2D COFs core/shell nanocubes with antiphotocorrosion ability for efficient photocatalytic hydrogen evolution, *Acs. Nano* 17 (2023) 5994–6001.
- [50] Y. Liu, S. Fu, D.L. Pastoetter, A.H. Khan, Y. Zhang, A. Dianat, S. Xu, Z. Liao, M. Richter, M. Yu, M. Polozij, E. Brunner, G. Cuniberti, T. Heine, M. Bonn, H. I. Wang, X. Feng, Vinylene-linked 2D conjugated covalent organic frameworks by wittig reactions, *Angew. Chem. Int. Ed.* 61 (2022), e202209762.
- [51] R.-R. Liang, S.-Y. Jiang, R.-H. A, X. Zhao, Two-dimensional covalent organic frameworks with hierarchical porosity, *Chem. Soc. Rev.* 49 (2020) 3920–3951.
- [52] W. Zou, G. Jiang, W. Zhang, L. Zhang, Z. Cui, H. Song, Z. Liang, L. Du, Hierarchically macro-microporous covalent organic frameworks for efficient proton conduction, *Adv. Funct. Mater.* 33 (2023) 2213642.
- [53] M. Liu, Y. Liu, J. Dong, Y. Bai, W. Gao, S. Shang, X. Wang, J. Kuang, C. Du, Y. Zou, J. Chen, Y. Liu, Two-dimensional covalent organic framework films prepared on various substrates through vapor induced conversion, *Nat. Commun.* 13 (2022) 1411.
- [54] W. Li, Z. Zhao, W. Hu, Q. Cheng, L. Yang, Z. Hu, Y.A. Liu, K. Wen, H. Yang, Design of Thiazolo[5,4-d]thiazole-bridged ionic covalent organic polymer for highly selective oxygen reduction to H<sub>2</sub>O<sub>2</sub>, *Chem. Mater.* 32 (2020) 8553–8560.
- [55] H. Wang, C. Yang, F. Chen, G. Zheng, Q. Han, A crystalline partially fluorinated triazine covalent organic framework for efficient photosynthesis of hydrogen peroxide, *Angew. Chem. Int. Ed.* 61 (2022), e202202328.
- [56] A. De, S. Haldar, S. Michel, L. Shupletsov, V. Bon, N. Lopatik, L. Ding, L.M. Eng, G. K. Auernhammer, E. Brunner, A. Schneemann, Manipulation of covalent organic frameworks by side-chain functionalization: toward few layer nanosheets, *Chem. Mater.* 35 (2023) 3911–3922.
- [57] C. Kang, Z. Zhang, A.K. Usadi, D.C. Calabro, L.S. Baugh, K. Yu, Y. Wang, D. Zhao, Aggregated structures of two-dimensional covalent organic frameworks, *J. Am. Chem. Soc.* 144 (2022) 3192–3199.
- [58] M. Liu, S. Yang, X. Yang, C.X. Cui, G. Liu, X. Li, J. He, G.Z. Chen, Q. Xu, G. Zeng, Post-synthetic modification of covalent organic frameworks for CO(2) electroreduction, *Nat. Commun.* 14 (2023) 3800.
- [59] M. Lu, J. Liu, Q. Li, M. Zhang, M. Liu, J.-L. Wang, D.-Q. Yuan, Y.-Q. Lan, Rational design of crystalline covalent organic frameworks for efficient CO<sub>2</sub> photoreduction with H<sub>2</sub>O, *Angew. Chem. Int. Ed.* 58 (2019) 12392–12397.
- [60] H. Ben, G. Yan, H. Liu, C. Ling, Y. Fan, X. Zhang, Local spatial polarization induced efficient charge separation of squaraine-linked COF for enhanced photocatalytic performance, *Adv. Funct. Mater.* 32 (2021) 2104519.
- [62] J. Xu, S. An, X. Song, Y. Cao, N. Wang, X. Qiu, Y. Zhang, J. Chen, X. Duan, J. Huang, W. Li, Y. Wang, Towards high performance Li-S batteries via sulfonate-rich COF-modified separator, *Adv. Mater.* 33 (2021), e2105178.
- [63] Y. Liu, W.-K. Han, W. Chi, J.-X. Fu, Y. Mao, X. Yan, J.-X. Shao, Y. Jiang, Z.-G. Gu, One-dimensional covalent organic frameworks with atmospheric water harvesting for photocatalytic hydrogen evolution from water vapor, *Appl. Catal. B* 338 (2023), 123074.